



HAL
open science

A damage criterion based on energy balance for isotropic cohesive zone model

André Chrysochoos, Loïc Daridon, Mathieu Renouf

► **To cite this version:**

André Chrysochoos, Loïc Daridon, Mathieu Renouf. A damage criterion based on energy balance for isotropic cohesive zone model. 2021. hal-03098095v4

HAL Id: hal-03098095

<https://hal.science/hal-03098095v4>

Preprint submitted on 21 Oct 2021 (v4), last revised 11 Mar 2022 (v5)

HAL is a multi-disciplinary open access archive for the deposit and dissemination of scientific research documents, whether they are published or not. The documents may come from teaching and research institutions in France or abroad, or from public or private research centers.

L'archive ouverte pluridisciplinaire **HAL**, est destinée au dépôt et à la diffusion de documents scientifiques de niveau recherche, publiés ou non, émanant des établissements d'enseignement et de recherche français ou étrangers, des laboratoires publics ou privés.

A damage criterion based on energy balance for an isotropic cohesive zone model

✉ André Chrysochoos^{1,2}, ✉ Loic Daridon^{1,2}, and ✉ Mathieu Renouf^{1,2}

¹ LMGC, Université de Montpellier, CNRS, Montpellier, France

² MIST, Université de Montpellier, IRSN, CNRS, France

1 The objective of this paper is to present an energy damage criterion for cohesive zone models (CZM) within the
2 framework of the non-linear thermodynamics of irreversible processes (TIP). An isotropic elastic damageable material
3 is considered for isothermal transformations. Damage is then the only irreversible effect accompanying the deformation
4 process and this mechanism is assumed to be fully dissipative. Once a separation law and a damage state variable
5 have been chosen, it is demonstrated that the damage evolution law can be automatically derived from the energy
6 balance. From this observation, a CZM is derived for a given choice of traction-separation law and damage state
7 variable and the quality of its numerical predictions is analyzed using an experimental benchmark bending test.
8 Damage, elastic and dissipated energy fields around the crack path are shown during this rupture test. Finally, a
9 numerical simulation of a Brazilian test is proposed where no pre-crack is present in the specimen. Then, as before,
10 the evolution of the dissipated energy fields are plotted during the loading until the total failure of the specimen.

11 Keywords cohesive zone, damage, fracture, thermodynamics of irreversible processes, energy balance, Finite element analy-
12 sis, Brazilian test

13

14 1 Introduction

15 In many industrial situations, the management of damage and failure of mechanical structures is crucial.
16 This is the reason why many academic and industrial laboratories have intensively studied and still study
17 this problem from an experimental, theoretical, and numerical point of view. Behavioral models taking
18 into account the damage, cracking and failure of structures have followed roughly two distinct paths.
19 Since the pioneering work of Dugdale [Dugdale 1960](#) and Barenblatt [Barrenblatt 1962](#), surface approaches
20 were proposed. Their objective was to describe in a practical way the material behavior during its rupture,
21 more precisely during the onset and the propagation of crack. The concept of traction-separation curve
22 associated with the crack tip was introduced to depict the gradual separation of material elements. This
23 type of approach has led to the so-called cohesive zone models. The other path can be characterized by
24 continuum damage approaches that have gradually developed since the works of Kachanov [Kachanov 1986](#)
25 and Rabotnov [Rabotnov et al. 1970](#). Volume descriptions have often used a scalar or tensorial damage
26 variable to describe the progressive degradation of the material. These variables are still often linked to the
27 loss of material elastic stiffness (e.g. [Lemaitre 1996](#)).

28 During these last thirty years, whether mechanical approaches are surface or volume, some have been
29 progressively presented within a thermodynamics of irreversible processes (TIP) framework. (e.g., [Costanzo](#)

30 [et al. 1995](#); [Chandrakanth et al. 1995](#)). Thermodynamics provides indeed a consistent framework both for
31 discussing the admissibility of the constitutive equations that account for the irreversibility of damage
32 mechanisms, and for characterizing the energy properties of damage and crack growth phenomena.
33 A significant number of works dealing with volume approaches used the TIP with internal variables
34 including state variables related to the damage. The behavioral constitutive equations are then divided into
35 two groups: the state equations derived from the thermodynamic potential, characterizing the properties
36 of equilibrium states of the material, and the complementary (or evolution) equations derived either
37 from threshold functions generally defined in the space of thermodynamic forces associated with the
38 model, or from a dissipation potential in the framework of Generalized Standard Materials [Kondo et al.](#)
39 [2007](#). Particular attention has been paid to the form of the evolution equations such that the model
40 predictions conform to the 2nd principle of thermodynamics. For cohesive zone models, the introduction
41 of thermodynamics has been much the same as for the bulk/continuum approaches. As [Costenzo et](#)
42 [al. Costanzo et al. 1995](#) noted, [Gurtin Gurtin 1979](#) was probably the first to propose a thermodynamic
43 framework for cohesive zones in fracture. He proposed to consider the crack surface as a two-dimensional
44 thermodynamic system endowed with a potential, (e.g., free energy), dependent on the crack temperature
45 and the crack tip opening displacement. Regarding the evolution laws, and particularly those related to
46 the damage variables, some, like [Costenzo et al. Costanzo et al. 1995](#) advocate the use of a dissipation
47 potential in the GSM framework. Others, probably more numerous, proposed forms of differential (kinetic)
48 equations. Although it is impossible to mention all the works related to how damage kinetics were
49 constructed, some references spanning the last 20 years include: [Ortiz and Pandolfi Ortiz et al. 1999](#), [Roe](#)
50 [et al. 2003](#), [Evangelista et al. Evangelista et al. 2013](#), [Serpieri et al. Serpieri et al. 2015a](#), [Kuna and Roth](#)
51 [Kuna et al. 2015](#), and more recently [Shu and Stanciulescu Shu et al. 2020](#). Here again, when the evolution
52 law is not derived from a dissipation potential, it is necessary to check that the irreversible evolution
53 of the system is in accordance with the second principle of thermodynamics, often formulated via the
54 Clausius-Duhem inequality.

55 In this paper, we focus on the formulation of a CZ model for an isotropic elastic damageable material.
56 Its main objective is to show that when the damage is the only irreversible mechanism and when this
57 latter is fully dissipative, it is no longer necessary to formulate any hypothesis concerning the damage
58 evolution law, this one being entirely fixed by the energy balance. The potential interest of such an
59 observation is that from now on, experimental techniques dealing with thermal and kinematic full-field
60 measurements allow one to evaluate local energy balances whose results will help to identify the CZ
61 model. [Richefeu et al. 2012](#).

62 The following sections are devoted to the construction of an energy damage criterion derived from the
63 energy balance for an isotropic elastic damageable material within the TIP framework. Contrary to what is
64 classically done, the damage kinetics is not derived, in this work, from an ad-hoc threshold criterion or
65 a dissipation potential but is based on the premise that the damage progress is linked to a prescribed
66 evolution in the maximum elastic energy that can be stored within the material for a given damage state.

67 From an energy standpoint, it must be noted that the damage mechanisms are considered as the only
68 microstructural irreversible effects accompanying the deformation process and these mechanisms are
69 fully dissipative (no energy storage induced by the material degradation). These restrictive hypotheses
70 are however often implicitly present in the literature we have previously mentioned. To illustrate this
71 statement, let us consider for example the paper proposed by Bouvard et al. [Bouvard et al. 2009](#). In
72 this paper, the fact that the damage is the only dissipative mechanism is described by a traction force
73 defined via a state law (i.e. no irreversibility is associated with the displacement jump). The fact that the
74 damage mechanisms are considered as fully dissipative can be established once looking at the dissipation
75 form: the dissipation is the product of the thermodynamic force associated with the damage multiplied
76 by the damage rate. In such a case, no energy storage (or release) accompanying the damage progress
77 should appear in the model simulations. Naturally, damage dissipation may induce self-heating leading to
78 non-isothermal deformation processes that are consequently irreversible due to heat diffusion. However,
79 for sake of simplicity, only isothermal transformations are considered in the following sections, and the
80 chosen state variables are the displacement jump vector \mathbf{u} and a scalar damage variable, denoted by u_d .
81 This damage variable u_d is the maximum of the equivalent opening displacement as used in many papers
82 such as [Ortiz et al. 1999](#), [Bosch et al. 2006](#), [Park et al. 2009](#), [Daridon et al. 2011](#), [Blal et al. 2011](#) for example.

83 The layout of the paper is as follows. The energy criterion of the damageable elastic cohesive zone
84 model is presented in Section 2 through a 1-D scenario within the TIP framework. In Section 3, a
85 vectorial extension of the cohesive zone law is proposed for an isotropic damage evolution. In Section
86 4, the capability of the model is investigated using an experimental benchmark test (i.e. a single-edge
87 notch-bending specimen for fracture toughness testing) [Moës et al. 2011](#); [Wojtacki et al. 2015](#); [Galvez et al.](#)
88 [1996](#). Mechanical and energy responses are shown and discussed. Several damage, elastic and dissipated
89 energy fields around the fracture paths are plotted during the crack propagation. As already mentioned,
90 the computation of the dissipated energy fields is of special interest since they can be compared with the
91 ones derived from quantitative IR techniques. The reader interested in these techniques can refer to
92 [Chrysochoos 2012](#); [Benaarbia et al. 2017](#). With this perspective, in the final section, a numerical simulation
93 of a Brazilian disc test is proposed. This kind of test is well adapted to infrared imaging since the flat
94 surface of the specimen remains perpendicular to the optical axis of the camera until the crack occurs.

95 **2 1D scenario**

96 The objective of the following section is to briefly review the mechanical concepts classically introduced
97 with CZM in the case of a 1D monotonic traction and to embed them into the TIP framework to derive,
98 through an energy criterion, a damage evolution law.

99 **2.1 Mechanical aspects**

100 In the literature, the mechanical response of the cohesive zone is described by the correspondence between
101 the “normal traction” force f supported by the interface and its normal opening displacement often called

102 “separation” during a monotonic opening. Depending on the chosen form of the traction-separation
 103 diagram, the relationships are called bilinear, polynomial or exponential cohesive laws. In Figure 1 a
 104 polynomial form has been chosen to illustrate the most commonly characteristics of these curves. We find
 105 the cohesive strength f_0 corresponding to the maximum of the traction–separation curve or its associated
 106 opening displacement u_0 , the maximum value of separation u_c corresponding to the crack opening. An
 107 energy parameter is also often mentioned [Ortiz et al. 1999](#): this is the fracture energy $A_c = \int_0^{u_c} f(u)du$
 108 (work of separation), which is the area below the traction-separation curve.

109 This traction-separation curve is considered as a threshold over which the damage develops irreversibly.
 110 This threshold is an intrinsic characteristic of the cohesive zone behavior. When unloading is considered,
 111 it is supposed to be purely elastic, assuming that the damage progress stops as soon as the loading point is
 112 below the threshold curve. For convenience, the elastic unloading paths are often directed towards the
 113 origin of the traction–separation diagram (see Figure 1). This implies that the elasticity remains linear and
 114 that there is no residual opening at the end of the unloading.

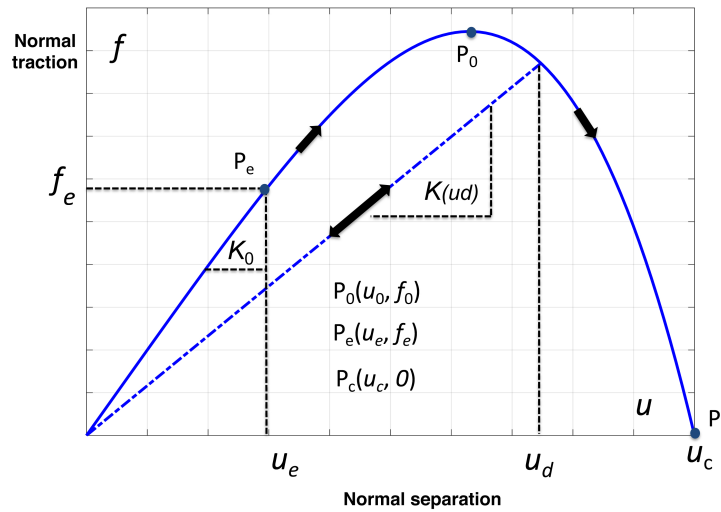


Figure 1: Traction-separation diagram. Monotonic envelope (continuous line), elastic unload or reload (dashed line). An arbitrary polynomial cohesive law has been chosen.

115 The progress of the damage can be depicted by a continuous decrease of the secant stiffness $K = \frac{f}{u}$
 116 towards zero until rupture at u_c . A classical scalar definition of the damage variable can then be given by:

$$D_k = \frac{K_0 - K}{K_0}, \quad (1)$$

117 where K_0 is the initial stiffness of the cohesive zone. The variable D_k progressively increases from 0 to
 118 1 when the opening displacement increases from 0 to u_c (or from u_e to u_c when a pure elastic domain,
 119 $[0, u_e]$, is introduced in the traction-separation curve (see Figure 1)).

120 A second possibility is to consider a normalized deformation energy definition of the damage [Ortiz](#)
 121 [et al. 1999](#) :

$$D_A = \frac{A}{A_c}, \text{ where } A = \int_0^u f(v)dv . \quad (2)$$

122 Here again, this last definition slightly changes when an elastic domain limited by the point (u_e, f_e) is
123 introduced. In such a case, *Eq.(2)* requires a renormalization:

$$D_A^* = \frac{A^*}{A_c^*}, \text{ where } A^* = \int_{u_e}^u f(v)dv \text{ and } A_c^* = \int_{u_e}^{u_c} f(v)dv . \quad (3)$$

Then by construction D_A and D_A^* belong to $[0, 1]$. In fact, there are many ways to define damage. The damage process being assumed irreversible, the damage variable rate is often chosen to be non-negative whatever the loading history, to depict its monotonic evolution. Damage develops when the mechanical state (u, f) corresponds to a point of the cohesive threshold curve. In what follows we have chosen a kinematic definition of the damage variable. Like previously done by numerous authors (e.g. [Serpieri et al. 2015b](#)), we have chosen the maximum value of the separation u_d ever reached by the cohesive zone until instant t . This damage state variable is then defined at instant t by:

$$u_d = \max \{u(\tau), \forall \tau \leq t\} . \quad (4)$$

124 This variable monotonically increases during the damage progress from 0 to u_c whatever the loading
125 path (see [Fig.1](#)).

126 2.2 Energy aspects

127 Usually during a load cycle, the deformation energy w_{def} , which corresponds to the area surrounded by
128 the loading curve *Eq.(7)* is transformed into dissipated energy, denoted by w_d , and stored energy, denoted
129 by w_s , due to the irreversible microstructural transformations accompanying the deformation process.
130 Part of w_{def} can also involve strong thermomechanical coupling energy (heat) w_{thm} [Chrysochoos 2012](#).
131 An illustrative example of the coupling effects on the mechanical response can be given by the famous
132 thermoelastic damping presented by Zener in [Zener 1938](#). The general form of the energy balance over a
133 loading cycle can then be written as:

$$w_{def} = w_d + w_s + w_{thm} . \quad (5)$$

134 For any other loading the elastic energy, w_e , has to be added so that :

$$w_{def} = w_e + w_d + w_s + w_{thm} , \quad (6)$$

135 w_e vanishing, by construction, over a loading cycle. In the present situation, we only consider
 136 isothermal transformations with no thermomechanical coupling. Moreover, we assume that damage is a
 137 pure dissipative mechanism and that, consequently, no energy storage or release of stored energy, due to
 138 microstructural changes, occurs during the loading. These assumptions imply $w_s = 0$ and $w_{thm} = 0$. For
 139 any kind of separation-controlled loading $\{u(\tau), \forall \tau \leq t\}$, the deformation energy at instant t is here
 140 defined by:

$$w_{def}(t) = \int_0^t f(\tau) \dot{u}(\tau) d\tau . \quad (7)$$

141 For monotonic loadings, the mechanical state follows the traction-separation curve. The deformation
 142 energy then represents the mechanical energy required to reach the damage state $u_d = u(t)$. This cost in
 143 deformation energy can be defined by:

$$w_{def}^d(u_d) = \int_0^{u_d} f(v) dv . \quad (8)$$

144 Another important mechanical energy term is the elastic energy, $w_e(u, u_d)$, in the cohesive zone at a
 145 given state of damage u_d . It is defined by:

$$w_e(u, u_d) = \frac{1}{2} K(u_d) u^2 . \quad (9)$$

146 Note that this energy is mechanically recoverable during the unloading. This is the reason why it did
 147 not appear in the general form of the energy balance proposed in Eq.(5) for a complete loading cycle.

148 As previously done for the deformation energy during monotonic loading, we can define the elastic
 149 energy $w_e^d(u_d)$ by:

$$w_e^d(u_d) = \frac{1}{2} K(u_d) u_d^2 = w_e(u_d, u_d) , \quad (10)$$

150 which represents the maximum elastic energy mechanically recoverable for a given damage state,
 151 defined by u_d .

152 As previously supposed (no thermomechanical coupling energy, no energy storage) the difference
 153 between $w_{def}^d(u_d)$ and $w_e^d(u_d)$ is attributed to the energy dissipation accompanying the irreversibility of
 154 damage mechanisms. The dissipated energy, $w_d^d(u_d)$, is then defined by :

$$w_d^d(u_d) = w_{def}^d(u_d) - w_e^d(u_d) , \quad (11)$$

155 $w_d^d(u_d)$, $w_e^d(u_d)$ and $w_{def}^d(u_d)$ are illustrated in Figure 2.

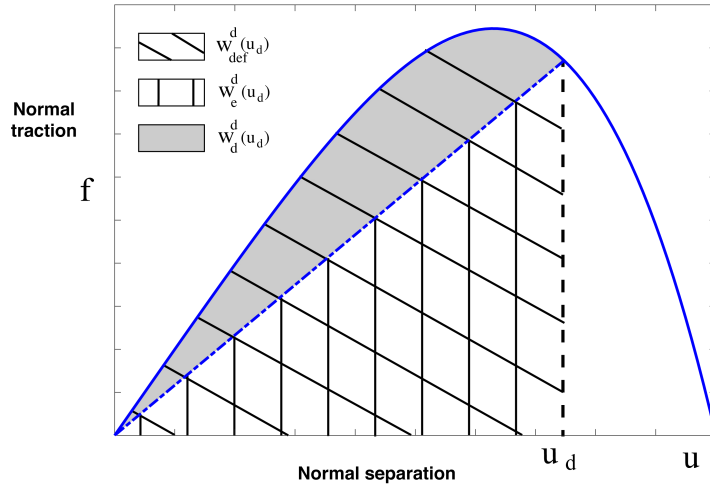


Figure 2: Energy illustration of the traction-separation diagram. Monotonic envelope (continuous blue line), elastic unload (dashed blue line).

156 Based on the mechanical response chosen in Figure 1, the evolutions of the three different energies
 157 associated with a loading-unloading tensile testing are shown in Figure 3. The deformation, elastic, and
 158 dissipated energies are plotted in green, blue, and red respectively. The deformation energy w_{def} is
 159 naturally the sum of the dissipated w_d and elastic w_e energies Eq.(6) since the damage is supposed to
 160 be the only microstructural transformation which is fully dissipative during loading, see Eq.(11) (no
 161 energy storage is induced by the microstructural transformations). Figure 3(a) illustrates that during the
 162 elastic unloading w_e^d remains constant (no evolution of damage) while w_e returns to zero. In parallel,
 163 the deformation energy w_{def} also decreases and tends towards the energy previously dissipated during
 164 the first loading cycle, w_d^d . In Figure 3(b) the elastic reloading while $u \leq u_d$ is shown (dashed lines) and
 165 extended by a monotonic loading until rupture for $u_d = u_c$ (full lines).

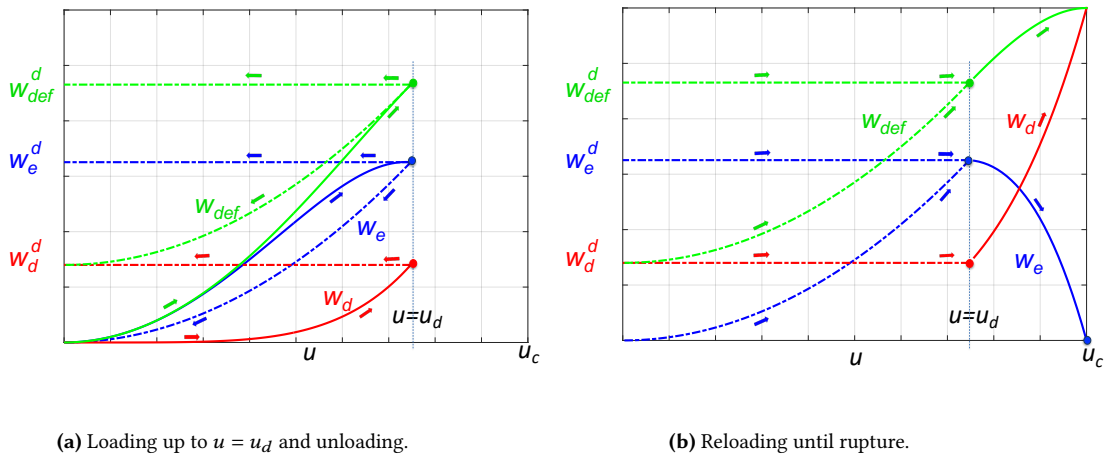


Figure 3: Energy balance evolution during a load-unload-reload process - Continuous lines are associated with the monotonic envelope, dashed lines correspond to the elastic unload and reload.

166 Under these restrictive assumptions, the area under the traction-separation curve, Figure 1 (equivalent
 167 to a monotonic traction rupture) is completely dissipated when the cohesive zone vanishes. In the next

168 sub-section once the thermodynamic working framework has been specified, this important property is
 169 discussed. Then, another point to underline is that if the traction-separation curve is classically considered
 170 as the constituent element of the behavior of the cohesion zone, it is thus the same for the evolutions of
 171 $w_{def}^d(u_d)$ and $w_e^d(u_d)$. Therefore, instead of using the tension-separation curve to describe the damage
 172 progress, associated with the loss of stiffness, it is also possible to use the evolution of the allowable
 173 maximum elastic energy w_e^d to define the threshold function associated with the damage rate.

174 2.3 Thermodynamics aspects

175 In this sub-section, the above results and comments are integrated into the TIP framework.

176 2.3.1 Cohesive zone potential and state laws

In the case of isothermal transformations, the chosen state variables are (u, u_d) . The thermomechanical approach starts with the assumption of the existence of a potential $\psi(u, u_d)$ capable of gathering all the state laws. Here we identify this potential to the elastic energy w_e defined in Eq.(10):

$$\psi(u, u_d) = \frac{1}{2}K(u_d)u^2. \quad (12)$$

177 The state laws are by construction the partial derivatives of the potential with respect to the state
 178 variables. We then define the conjugate variable f^r , associated with u which represents the reversible part
 179 of the traction force, and A_d the conjugate variable associated with u_d respectively :

$$\left\{ \begin{array}{l} f^r = \frac{\partial \psi}{\partial u} = K(u_d)u \\ A_d = \frac{\partial \psi}{\partial u_d} = \frac{1}{2}K'(u_d)u^2 \end{array} \right., \quad (13)$$

180 where $K'(u_d) = \frac{dK(u_d)}{du_d}$.

181 2.3.2 Clausius-Duhem inequality

The irreversibility of the mechanisms accompanying the opening of the cohesive zone is depicted by the Clausius-Duhem inequality which enables the definition of the intrinsic dissipation w_d^o . In the present framework, it can be written as :

$$w_d^o = w_{def}^o - \dot{\psi} = f\dot{u} - \frac{\partial \psi}{\partial u}\dot{u} - \frac{\partial \psi}{\partial u_d}\dot{u}_d = f^{ir}\dot{u} + X_d\dot{u}_d \geq 0. \quad (14)$$

182 The terms w_d^o and w_{def}^o determine the dissipated and deformation energy rates, respectively. The symbol
 183 $(-)^o$ is introduced to underline that w_d and w_{def} are not a priori state functions and are then path
 184 dependent. Eq.(14) also introduce the irreversible part of the traction force, $f^{ir} = f - f^r$, and the
 185 thermodynamic force X_d associated with \dot{u}_d . Note that during an irreversible transformation $\dot{u}_d > 0$ we
 186 get $X_d = -A_d$. If damage is the only irreversible process, no dissipation has to be associated with \dot{u} . In

187 such a case the irreversible traction force vanishes $f^{ir} = 0$. The traction force f can then be directly
 188 defined via the state law:

$$f = f^r = K(u_d)u . \quad (15)$$

189 Moreover, the intrinsic dissipation becomes with Eq.(13) and Eq.(14) :

$$w_d^o = X_d \dot{u}_d = -\frac{1}{2} K'(u_d) u^2 \dot{u}_d \geq 0 . \quad (16)$$

190 The fact that $\dot{u}_d \geq 0$ implies $K'(u_d) \leq 0$ what is physically consistent. The irreversible nature of
 191 damage leads to a degradation of the secant stiffness.

192 2.3.3 Threshold function and damage evolution law

193 In the TIP framework the thermodynamic forces are supposed to be function of the state variable rates. In
 194 the case of the linear TIP proposed by Onsager [Onsager 1931](#), the correspondence between thermodynamic
 195 forces and state variable fluxes is linear. The Onsager matrix is supposed to be symmetric positive definite
 196 in order to verify the Clausius-Duhem inequality (positive dissipation) whatever the thermodynamic
 197 process. Extension to non-linear theory exists as for example the formalism of Generalized Standard
 198 Materials [Halphen et al. 1975](#). Based on the hypothesis of normal dissipation, the thermodynamic forces
 199 derive from a convex dissipation potential or equivalently, state variables rates derived from a dual
 200 dissipation potential, function of the thermodynamic forces. This dissipation potential can also involve the
 201 state variables of the model as parameters [Lemaitre 1996](#). A common approach is then:

- 202 - to define a threshold function depending on the thermodynamic forces (and possibly state variables)
- 203 - to write that irreversibility occurs and develops if the thermodynamic state is on the threshold and
 204 remains on it during a time increment.

205 Note that once the state laws (derived from the thermodynamic potential) and complementary laws
 206 (derived from the dissipation potential) have been written, it is then possible to deduce the evolution of the
 207 energy balance associated with the transformation.

In what follows the existence of the threshold function will not be associated with the normal
 dissipation hypothesis as the energy balance form imposes by construction non-negative dissipation.
 Indeed, the current elastic domain is characterized by $w_e^d(u_d)$ the maximum elastic energy available for a
 given damage state which also corresponds to the energy required to further damage the material. Then
 the damage energy criterion based on the energy balance is defined by :

$$w_e(u, u_d) \leq w_e^d(u_d) . \quad (17)$$

208 The evolution law for u_d is then derived from the fact that for the damage to occur the maximum

209 elastic energy allowable in the material has to be and remain on the threshold during the loading step, i.e.

$$\begin{cases} w_e(u, u_d) = w_e^d(u_d) & \text{(a)} \\ \dot{w}_e(u, u_d) = \dot{w}_e^d(u_d) & \text{(b)} \end{cases} . \quad (18)$$

210 The first equality gives naturally $u_d = u$. The second equality leads to a proposal of evolution equation
211 for the damage :

$$\dot{u}_d = \begin{cases} \dot{u} & \text{if } u = u_d \text{ and } \dot{u} \geq 0 \\ 0 & \text{if } u < u_d \text{ or } \dot{u} \leq 0 \end{cases} , \quad (19)$$

212 what is consistent if we remind the definition of the damage state variable *Eq.(4)* and the fact that the
213 damage increases irreversibly, $\dot{u}_d \geq 0$.

214 To be fully compatible with non-linear TIP framework, the final step is to propose a threshold function
215 that takes the thermodynamic force X_d into account. As previously stated, we consider a derivative form
216 of the energy balance to get this threshold function *Eq.(18)b*. By using *Eq.(13)* and *Eq.(16)*, we get:

$$\frac{d w_e}{dt} = -X_d \dot{u}_d + K(u_d) u \dot{u} . \quad (20)$$

217 On the threshold, *Eq.(20)* becomes :

$$\frac{d w_e^d}{d u_d} \dot{u}_d = (-X_d + K(u_d) u_d) \dot{u}_d . \quad (21)$$

218 Then a threshold function F involving the thermodynamic force X_d and the state variables can be
219 taken under the form :

$$F(X_d; u, u_d) = K(u_d) u - X_d - \frac{d w_e^d}{d u_d} \leq 0 . \quad (22)$$

220 To be consistent with the incremental form of the energy balance, the equality $F(X_d; u, u_d) = 0$, gives
221 once again $u_d = u$ while the consistency condition $dF = 0$ leads to $du = du_d$, or equivalently to *Eq.(19)*.

222 To be precise, the full calculation of $dF = 0$ at $u = u_d$ leads to:

$$(K(u_d) + 2 K'(u_d) u_d) (du - du_d) = 0 , \quad (23)$$

223 then $du = du_d$, except possibly when $u_d = -\frac{K(u_d)}{2K'(u_d)}$.

224 2.3.4 Some comments about the damage evolution equations

225 To depict the evolution of damage, in addition to the traction-separation curve data, the literature often
 226 proposes a specific evolution equation in the form of $\dot{D} = \dot{D}(f, D, \dot{u})$ whatever the definition of the damage
 227 variable D [Roe et al. 2003](#); [Bouvard et al. 2009](#); [Kuna et al. 2015](#).

228 In the foregoing, because of the hypotheses explicitly made on the energy balance (i.e. damage is
 229 the only dissipative mechanism and it is totally dissipative), the damage evolution law is fixed by the
 230 definition of the damage variable itself and by the explicit form of the energy balance. Note that the
 231 damage evolution law [Eq.\(19\)](#) deduced from the energy criterion [Eq.\(18\)](#) is perfectly compatible with the
 232 definition of the damage variable itself given in [Eq.\(4\)](#). We can also note that this evolution law is an
 233 extremely simple form of the general equation proposed by [Roe et al. 2003](#), but here this law is totally
 234 imposed by the shape of the traction-separation curve or equivalently by the threshold $w_e^d(u_d)$ of [Eq.\(10\)](#)

To set ideas, let's consider the following simple case: let $f(u)$ be a 1D traction-separation law. We suppose that the elastic energy is, as often, written as: $\psi(u, D) = (1 - D)K_0 \frac{u^2}{2}$, where D is the isotropic damage variable, u the displacement jump, and K_0 the elastic stiffness of the virgin cohesive zone. We consider a monotonic loading. The deformation energy rate is given by definition:

$$\frac{dw_{def}}{dt} = f(u) \frac{du}{dt},$$

where $f(u)$ follows the traction-separation curve. The elastic energy rate can be split in two parts:

$$\frac{dw_e}{dt} = (1 - D)K_0 u \frac{du}{dt} - K_0 \frac{u^2}{2} \frac{dD}{dt}.$$

If we assume now that the damage is the only irreversible mechanism, then the traction force is the conjugate variable of the displacement jump, where $f(u) = \frac{\partial \psi(u, D)}{\partial u} = (1 - D)K_0 u$ and $\frac{dw_e}{dt} = \frac{dw_{def}}{dt} - K_0 \frac{u^2}{2} \frac{dD}{dt}$.

If now the damage is supposed to be exclusively dissipative (no internal stored energy), then the dissipation is given by:

$$\frac{dw_d}{dt} = K_0 \frac{u^2}{2} \frac{dD}{dt} = \frac{dw_{def}}{dt} - \frac{dw_e}{dt}.$$

Following the traction-separation curve, the damage evolution has to verify:

$$\frac{dD}{dt} = 2 \frac{\left(\frac{dw_{def}}{dt} - \frac{dw_e}{dt} \right)}{\frac{1}{2}K_0 u^2}.$$

Noting that for each current point $(u, f(u))$ of the traction separation curve, we have $w_e = \frac{1}{2}f(u)u$, the time derivation, following the curve, reads :

$$\frac{dw_e}{dt} = \frac{1}{2}f(u) \frac{du}{dt} + \frac{1}{2} \frac{df(u)}{dt} u.$$

Then,

$$\frac{dD}{dt} = \frac{f(u) \frac{du}{dt} - \frac{df(u)}{dt} u}{\frac{1}{2} K_0 u^2} .$$

235 The right-hand member of this equation is fully determined by the traction-separation curve. Any form of
 236 damage evolution law, incompatible with this previous equation, would lead to an energy balance form
 237 incompatible with the initial energy assumptions (i.e. form of the free energy, damage unique and exclusive
 238 dissipative mechanism). The consequences could be the appearance of energy storage mechanisms, i.e.
 239 $\dot{w}_d^d < \dot{w}_{def}^d - \dot{w}_e^d$, or internal energy transformation into dissipated energy (release of stored energy), i.e.
 240 $\dot{w}_d^d > \dot{w}_{def}^d - \dot{w}_e^d$. Taking into account this stored energy variations should lead to the introduction of new
 241 internal state variables and/or to a change of the deformation energy rate definition [Fremond 2002](#).

242 3 3D cohesive zone model

243 In this paragraph, we propose an extension to a 3D vectorial version of the CZM where the isotropic
 244 damage is controlled by the evolution of the maximum recoverable elastic energy, $w_d^e(u_d)$. Isotropic
 245 damage means here that a scalar state variable is solely used to describe the damage evolution. This
 246 generalization has been made by following the same approach as the one previously proposed, namely
 247 define a damage variable and a energy balance where the damage is the only dissipative phenomenon.

248 3.1 Mechanical variables

249 Regarding the mechanical description of the cohesive zone, the traction force and the separation become
 250 now vectors. Let us introduce a frame of reference where directions 1 and 2 correspond to the tangent
 251 plane of the cohesive zone while direction 3, is the normal direction. The traction vector, \mathbf{f} , whose
 252 components are (f_{t_1}, f_{t_2}, f_n) and the separation vector, \mathbf{u} , which has 3 components denoted by (u_{t_1}, u_{t_2}, u_n)
 253 are introduced. As is conventionally admitted in CZM, the normal move jump denoted by u_n is positive
 254 or null. This unilateral condition is taken into account by a Signori type relationship in the numerical
 255 simulations, using the open source software `LMGc90` [Dubois et al. 2006](#), performed at the end of this article.

256 3.2 Cohesive zone potential and state equations

A set of state variables has first to be chosen. Here we selected the components (u_{t_1}, u_{t_2}, u_n) of the
 separation vector and a scalar damage variable denoted by u_d . Then, to generalize the form of the cohesive
 zone potential proposed in [Eq.\(12\)](#), the following form, inspired by [Bouvard et al. 2009](#), is adopted :

$$\begin{aligned} \psi(\mathbf{u}, u_d) &= w_e(\mathbf{u}, u_d) \\ &= \frac{1}{2} \left(K_n(u_d) u_n^2 + K_t(u_d) u_{t_1}^2 + K_t(u_d) u_{t_2}^2 \right) \\ &= \frac{1}{2} K_n(u_d) (u_n^2 + \alpha u_{t_1}^2 + \alpha u_{t_2}^2) \\ &= \frac{1}{2} K_n(u_d) u_{eq}^2 \end{aligned} \tag{24}$$

where:

$$u_{eq} = (u_n^2 + \alpha u_{t_1}^2 + \alpha u_{t_2}^2)^{\frac{1}{2}}. \quad (25)$$

257 The parameter α is the ratio between $K_t(u_d)$, the tangential and $K_n(u_d)$, the normal secant stiffnesses
 258 at a given u_d . In the case of isotropic damage α is a constant.

259 In Eq.(26), a 3D formulation of the scalar depicting the isotropic damage is given. By construction, u_d
 260 takes the 3D aspect of the separation vector \mathbf{u} into account and then \dot{u}_d is non-negative and de facto
 261 respects the irreversibility of the damage progress.

$$u_d = \max \{u_{eq}(\tau), \forall \tau \leq t\}. \quad (26)$$

262 By definition, the state laws are the partial derivatives of the cohesive zone potential Eq.(24). They
 263 introduce the components of the reversible traction vector \mathbf{f}^r and the conjugate variable A_d associated
 264 with (u_{t_1}, u_{t_2}, u_n) and u_d respectively :

$$\begin{cases} f_n^r &= \frac{\partial \psi}{\partial u_n} &= K_n(u_d)u_n \\ f_{t_1}^r &= \frac{\partial \psi}{\partial u_{t_1}} &= \alpha K_n(u_d)u_{t_1} &= K_t(u_d)u_{t_1} \\ f_{t_2}^r &= \frac{\partial \psi}{\partial u_{t_2}} &= \alpha K_n(u_d)u_{t_2} &= K_t(u_d)u_{t_2} \\ A_d &= \frac{\partial \psi}{\partial u_d} &= \frac{1}{2}K'(u_d)u_{eq}^2 \end{cases}. \quad (27)$$

265 Because only damage induces irreversibility, no dissipation has to be associated with the component of
 266 the separation vector. The reversible part \mathbf{f}^r of the separation can therefore be identified with \mathbf{f} , then
 267 $\mathbf{f} = \mathbf{f}^r$.

268 3.2.1 Energy definition of the damage threshold

269 To extend the damage energy criterion to a 3D isotropic damageable CZM, it is possible to choose the
 270 damage variable, u_d , whose evolution is directly related to that of the elastic energy w_e^d . In the 3D case, this
 271 maximum elastic energy, for a given damage state u_d , describes in the displacement space a half spheroid of
 272 radii $r_n(u_d) = \left(\frac{2w_e^d(u_d)}{k_n(u_d)}\right)^{\frac{1}{2}}$ and $r_t(u_d) = \left(\frac{2w_e^d(u_d)}{\alpha k_n(u_d)}\right)^{\frac{1}{2}} = \frac{r_n(u_d)}{\sqrt{\alpha}}$ as shown in Figure 4. As the normal jump
 273 denoted u_n is by definition positive or null only half of the spheroid is reachable for any separation states.

274 As long as the further separation states, \mathbf{u} , respect the damage energy criterion (i.e. $w_e(\mathbf{u}, u_d) <$
 275 $w_e^d(u_d)$), the behavior remains elastic. Then for a given opening such that $u_{eq} = u_d$, the elastic energy
 276 reaches the maximal value associated with this damage state (i.e. $w_e(\mathbf{u}, u_d) = w_e^d(u_d)$). Once the surface
 277 of the spheroid is reached:

278 • either the separation increment $\delta \mathbf{u}$ is directed towards the inside of the spheroid, and an elastic

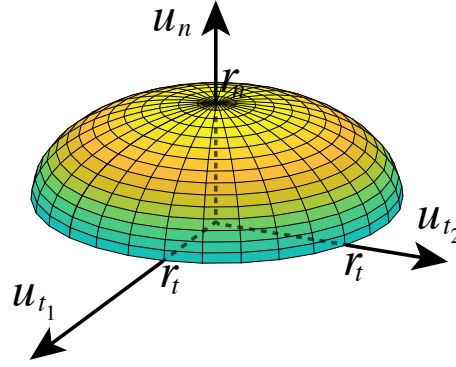


Figure 4: 3D representation of the reachable separation states for a given damage state u_d . The color variation represents the value of u_n .

279 unloading at constant damage can be observed,

280 • or $\delta \mathbf{u}$ is directed towards the outside of the spheroid, and then the damage develops defining a new
281 elastic limit surface.

282 For isotropic damage, a single evolution equation for u_d is required. We have already underlined that for
283 threshold behavior law, the yield function depends on the thermodynamic forces and possibly on the states
284 variables themselves, acting as parameters. In the present case, the thermodynamic force of the model,
285 associated with the damage variable rate, is X_d . A generalized form of the yield criterion proposed in
286 Eq.(22) is chosen where the role of u used in the 1D scenario is played by u_{eq} . So, the proposed yield
287 energy criterion Eq.(17), may be rewritten using the thermodynamic force, X_d as:

$$F(X_d; u_{eq}, u_d) = K_n(u_d) u_{eq} - X_d - \frac{d w_e^d}{d u_d} \leq 0. \quad (28)$$

288 Damage develops if the threshold is reached, $F(X_d; u_{eq}, u_d) = 0$ and if the consistency condition is
289 verified, $\dot{F}(X_d; u_{eq}, u_d) = 0$. For the same reasons as the ones shown for the 1D model, the evolution law of
290 the parameter u_d is written as:

$$\dot{u}_d = \dot{u}_{eq} \text{ if } u_d = u_{eq} \text{ and } \dot{u}_{eq} \geq 0, \quad (29)$$

291 results which, as already underlined, are imposed by the very definition of the damage variable.

292 An illustration of the energy criteria is given in Figure 5. Following a monotonic loading (i.e. remaining
293 on the $w_e^d(u_d)$ curve), $K_n(u_d)u_d$ is the slope of the deformation energy w_{def}^d , X_d is the slope of the
294 dissipated energy w_d^d and $(w_e^d)'$ is naturally the slope of the maximal allowable elastic energy w_e^d .

295 To conclude section 3, we would like to stress once more the fact that the damage evolution law is not
296 here a matter of choice. It is imposed by the chosen form of the energy balance and by the definition of the
297 damage state variable.

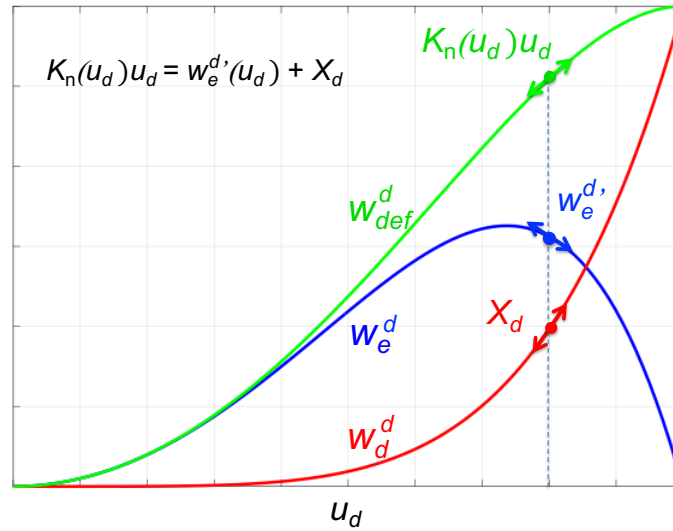


Figure 5: Illustration of the damage energy criterion - $u_{eq} = u_d$

298 The state equations Eqs(27) and the evolution equation Eq.(29) will be, in what follows, implemented
 299 in a home-made finite element code. The different material parameter of the constitutive equations will be
 300 specified. In order to show the capabilities of such a CZM, two types of simulations are made here after.
 301 The first one is a bending test whose numerical results are compared with experimental one's. The second
 302 one is a Brazilian disc test whose the material is made of heterogeneous elastic grains.

303 4 Numerical Implementation

304 To illustrate the potentiality of the proposed model, simulations reproducing a common benchmark
 305 extracted from the literature Galvez et al. 1996 were carried out. It is important to notice that the objective
 306 of this practical comparison is simply to show the operability of the model and not to optimize its
 307 parameters in order to fit the benchmark. The numerical implementation of the previous model is then
 308 done in the code LMGc90 based on Non-Smooth Contact Dynamics (NSCD) Moreau 1988; Jean 1999; Jean
 309 et al. 2001. The NSCD method is dedicated to solving problems related to dynamic systems with unilateral
 310 constraints. It is therefore particularly suitable for contact friction problems. It proposes a non-smooth
 311 treatment (no compliance, no penalty) of the conditions of contact Jean 1999, which is explicit in the
 312 definition of u_n . The way which adhesion is taken into account in this method makes it possible to
 313 consider each point of contact as a cohesive zone. Then the mechanical behavior of the cohesive zones
 314 may vary at any point of the spatial discretization of the problem. This relevant modeling framework was
 315 then adopted to numerically simulate crack propagation with cohesive zone Champagne et al. 2014 .

316

317 4.1 Bending test

318 To compare the proposed model with a benchmark found in literature Galvez et al. 1996, the form of the
 319 maximum storable elastic energy, which we remember is $w_e^d(u_d)$, must be specified in order to be able to

320 implement it in LMgc90, the open source platform¹ used to carry out the simulations Dubois et al. 2011.
 321 This benchmark, illustrated Figure 6, traces the evolution of a crack in mixed mode to be followed. In the
 322 context of this feasibility study, a simple quadratic form of $w_e^d(u_d)$ is proposed. In what follows, we also
 323 assumed the existence of a pure elastic domain and thus the existence of a threshold equivalent elastic
 324 displacement u_{eq}^e , simply denoted by u_e . The maximum storable elastic energy as a function of the damage
 325 parameter u_d simply reads:

$$w_e^d(u_d) = A(u_d - u_c)^2 + B(u_d - u_c), \text{ if } u_e \leq u_d \leq u_c, \quad (30)$$

where u_c is the critical equivalent displacement corresponding to the crack onset. Parameters A and B are two constants chosen to ensure the C_1 continuity of the maximum storable elastic energy, $w_e^d(u_d)$, at the threshold equivalent elastic displacement, $w_e^d(u_e) = \frac{1}{2} K_n^0 u_e^2$. They are defined by:

$$\begin{cases} A = -\frac{1}{2} K_n^0 u_e \frac{(2u_c - u_e)}{(u_c - u_e)^2} \\ B = -K_n^0 \frac{u_c u_e}{u_c - u_e} \end{cases}, \quad (31)$$

326 where K_n^0 is the initial normal stiffness of the CZM.

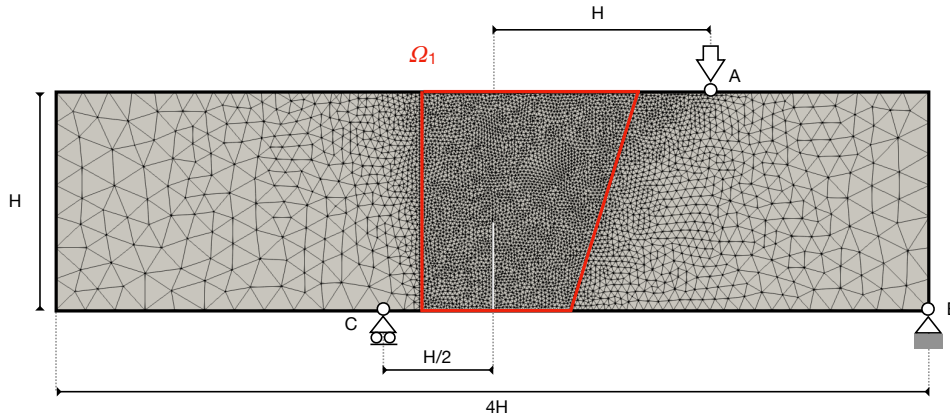


Figure 6: Characteristics of the benchmark issued from Galvez et al. 1996 used for simulation

327 The thickness of the sample, denoted by H , is equal to 0.3 m while its length is equal to 1.2 m. A 0.15 m
 328 pre-crack is located in the middle on the lower edge. The point B is fixed in both x and y directions
 329 whereas the point A is only fixed in the y direction. A displacement is imposed on the point A to load
 330 the structure. The mesh is composed of 3 parts: Two coarse meshes, the left and the right parts of the
 331 structure composed respectively of 958 and 2 063 T3 elements, where no interface elements have been
 332 introduced between the different meshes and a finer mesh, assuring the continuity of the structure (domain
 333 Ω_1 in Figure 6), composed of 6 723 T3 elements where the crack path is supposed to appear and where
 334 interface elements are therefore introduced between each element. The interactions between elements of
 335 Ω_1 are governed by the proposed cohesive zone model where the initial secant elastic stiffness, K_n^0 and K_t^0 ,

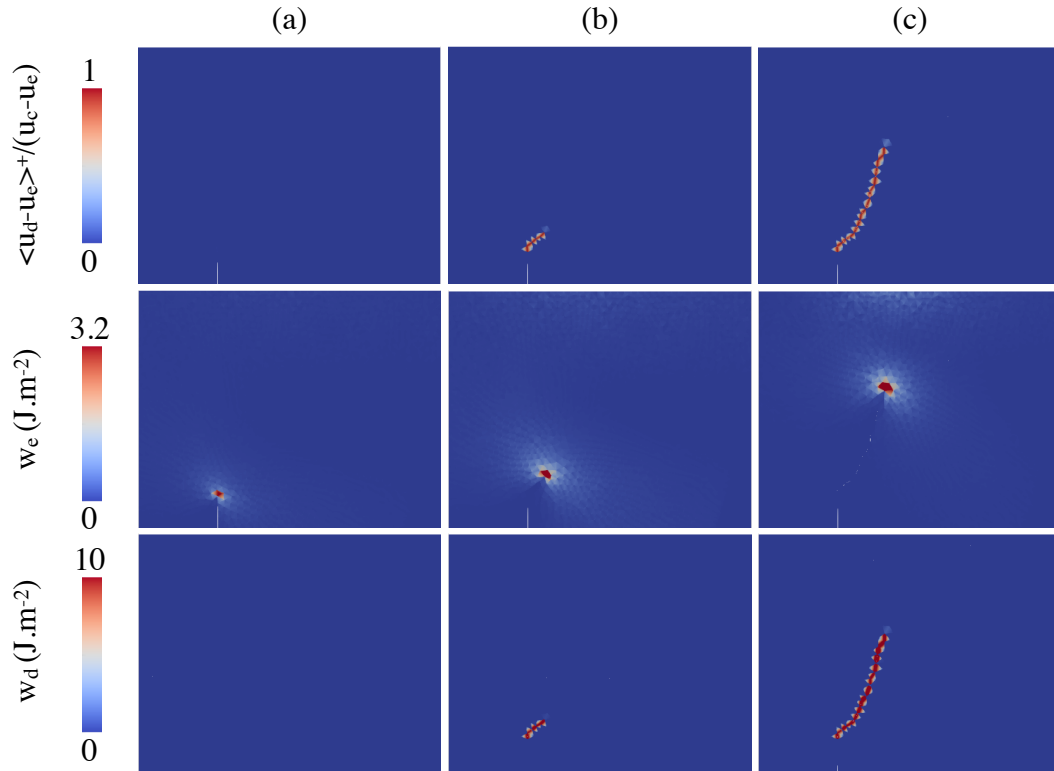
¹ <https://git-xen.lmgc.univ-montp2.fr/lmgc90/>

K_n^0 (N m ⁻¹)	α	u_e (m)	u_c (m)
$2.48 \cdot 10^9$	0.5	$0.5 \cdot 10^{-6}$	$1.5 \cdot 10^{-6}$

Table 1: Parameter values of the CZM

336 are chosen to satisfy the criterion proposed in [Blal et al. 2011](#) to limit the reduction of stiffness due to the
 337 presence of CZM. It is important to underline that the objective of this practical comparison is simply to
 338 show the operability of the model and not to optimize its parameters in order to fit the benchmark. The
 339 values of the CZM parameters are summarized in [Table 1](#).

340 [Figure 7](#) shows the evolution, for different simulation times, of different characteristic quantities
 341 associated with the model : the damage variable, the elastic energy w_e and the dissipated energy w_d . In
 342 order to present a quantity varying from 0 to 1 the damage ratio, as a function the damage variable, is
 343 introduced and defined by $\frac{\langle u_d - u_e \rangle^+}{u_c - u_e}$. To improve the visibility of these different quantities supported by
 344 the interfaces, they are projected on adjacent elements.

**Figure 7:** Visualization of the damage ratio (top row), the elastic energy (center) and the dissipated energy (bottom row) during the crack propagation

345 [Figure 7\(a\)](#), corresponding to a pre-cracking state, shows a concentration of the elastic energy at the
 346 outset of the crack tip. However, the damage criterion has not been reached within the cohesive zone so
 347 that no damage or dissipation has yet occurred (see [Eq.\(17\)](#)). The corresponding map to $\frac{\langle u_d - u_e \rangle^+}{u_c - u_e}$ and w_d
 348 are then uniformly equal to 0. As expected, [Figure 7 \(b\) and \(c\)](#), corresponding to two post-cracking steps,
 349 highlight the correlation between the evolution of the dissipated energy and the damage ratio. The elastic
 350 energy is still concentrated ahead of the crack tip, then returns to zero along the crack lips. In contrast, the
 351 dissipated energy related to the damage evolution can be exhibited all along the crack path. Similarly, the

352 damage field allows the cracking path to be tracked.

353 To exhibit the capability of our CZM where only the shape of the cohesive energy associated with a
 354 simple energy balance is needed (cf. *Eq.(30)*), different quantities, numerically obtained, are compared with
 355 experimental measurements present in the literature [Cendón et al. 2000](#). For such comparisons, Figure 8
 356 presents both the classical crack path monitoring and the load vs. CMOD curve (Crack Mouth Opening
 357 Displacement).

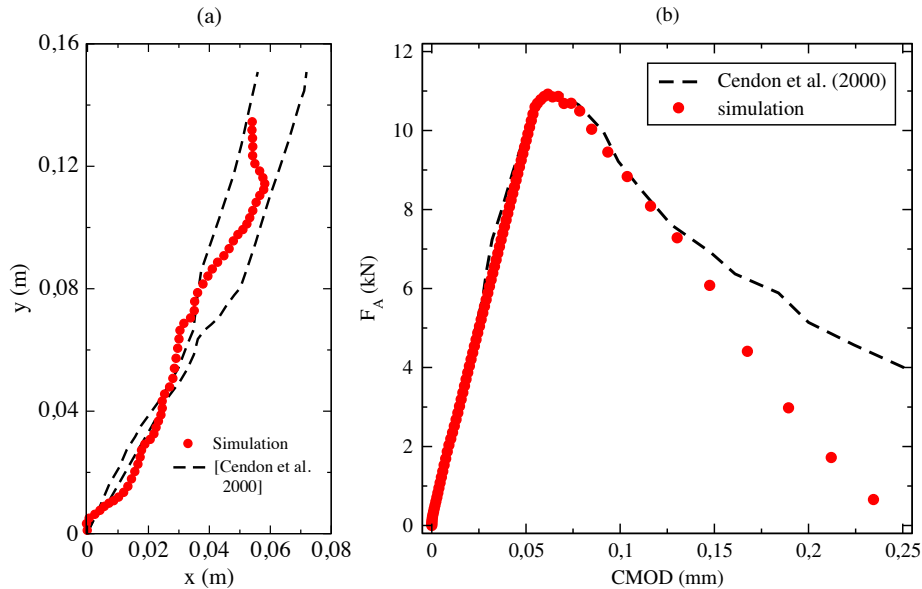


Figure 8: Comparison of numerical macroscopic measurements associated to the crack evolution with experimental results [Cendón et al. 2000](#): a) The crack path and b) the load vs. CMOD curve.

358 In Figure 8(a) and Figure 8(b), the red dot line corresponds to the simulation result while the black
 359 dashed lines represent the crack envelop obtained experimentally [Cendón et al. 2000](#). In Figure 8a, the
 360 crack obtained numerically corresponds closely to the experimental envelope. The starting angle is
 361 strongly related to the discretization around the initiation point, explaining the slight difference at the
 362 beginning of the initiation. Then, the path is corrected and repositioned in the experimental envelope until
 363 the end of the simulation.

364 Concerning the force vs. CMOD curves, they fit perfectly in the section corresponding to the linear
 365 increase. This highlight that the introduction of a 2D interface element, where the values of K_n^0 and K_t^0
 366 satisfy the criterion proposed in [Blal et al. 2011](#) between each elements of Ω_1 do not affect the global
 367 stiffness of the sample. The maximum force obtained is also in good agreement with that obtained in the
 368 experiment, as well as the beginning of the non-linear decreasing part of the CMOD curve occurring at the
 369 initiation of cracking. In the last part, the curves diverge. This difference is partly explained by the fact that
 370 the numerical simulation is two-dimensional while the experiments are three-dimensional. Indeed, not all
 371 deformation modes are taken into account (especially out-of-plane modes), which explains this different
 372 behavior at the end of the simulation. Moreover, we have arbitrarily chosen a 2nd degree polynomial to
 373 characterize the damage of the cohesive zone model, *Eq.(30)*. This choice could be fine-tuned in order to
 374 better account for experiences by taking a Needleman-type damage, [Bosch et al. 2006](#); [Needleman 1990](#).

375 4.2 Sensitivity study

376 Finally, in order to see the impact of a variation in the parameters u_e and u_c on the overall behavior of
 377 the system and more particularly on the evolution of the force vs. CMOD curves, a sensitivity study is
 378 proposed. The influence of these parameters on the crack path is not presented because it is not very
 379 significant. The influence of these parameters on the energy available to be dissipated in the model
 380 is pointed out in Figure 9. The parametric study is carried out relative to the reference point (0, 0)
 381 corresponding to the results presented in Figure 8(b) with the parameters define in table 1. With the chosen
 382 law, a variation of u_c has almost the same consequence as a variation of u_e in terms of the energy available
 383 to be dissipated. Then the map presented in Figure 9 is symmetric in the regard of the circle-triangle
 384 diagonal. During the different parametric studies, the color code used for the curves will refer to the one
 385 defined in Figure 9.

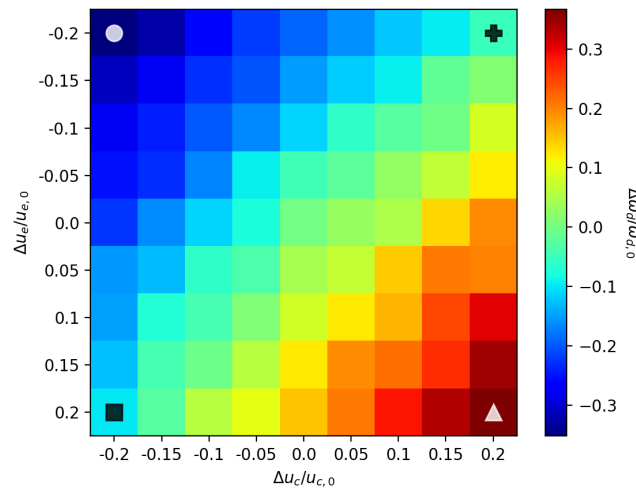


Figure 9: Map of the normalized dissipated energy variations as a function of the variations of u_e and u_c . The symbols used at the four corners of the map identify the curves shown in Figure 10.

386 Figure 10 presents the normalized plots of $w_e^d(u_d)$ for different values of u_e and u_c (Figure 10(a)) and the
 387 corresponding force vs. CMOD curves (Figure 10(b)). The normalization parameters are $u_{e,0} = 0.5 \cdot 10^{-2}$ and
 388 $w_{e,0} = w_{e,0}^d(u_{e,0})$ using the values of parameters in Tab. 1. Even if the shape of the curves is significantly
 389 different in Figure 10 (a), the energies available to be dissipated for the case represented by a cross and the
 390 one represented by a square are of same order of magnitude. The maxima order observed at the scale of
 391 the CZM models (Figure 10(a)) is conserved at the scale of the structure (Figure 10(b)).

392 In Figures 11 to 13, we observe respectively the influence of u_c and u_e on the force vs. CMOD curves.
 393 These figures show that the influence of the variation of u_c is less than that of u_e . Indeed, where we
 394 observe for a variation of u_c a variation of less than 10% on the critical values of the curve (F_{max} and
 395 $CMOD_{max}$), while a variation of more than 20% for an equivalent variation of u_e is observed. Nevertheless,
 396 in both cases, an increase of the damage energy w_d induces an increase of the CMOD and loading maxima
 397 in the Load vs. CMOD curve. In this model where an elastic domain is assumed, u_e is the threshold where
 398 the damage begins to occur. This value determines the outset of the non-linear response of the structure.

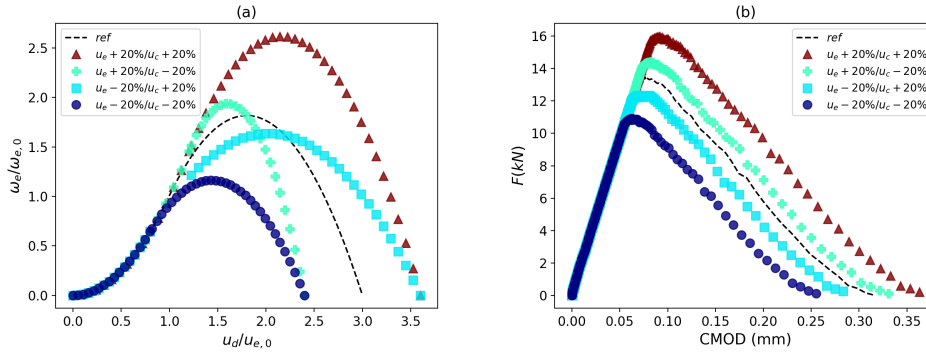


Figure 10: (a) Normalized plots of $w_e^d(u_d)$ for different values of u_e and u_c . The normalization parameters are $u_{e,0} = 0.5 \cdot 10^{-2}$ and $w_{e,0} = w_e^d(u_{e,0})$ using the values of parameters in Tab.1. (b) Corresponding force vs. CMOD curves.

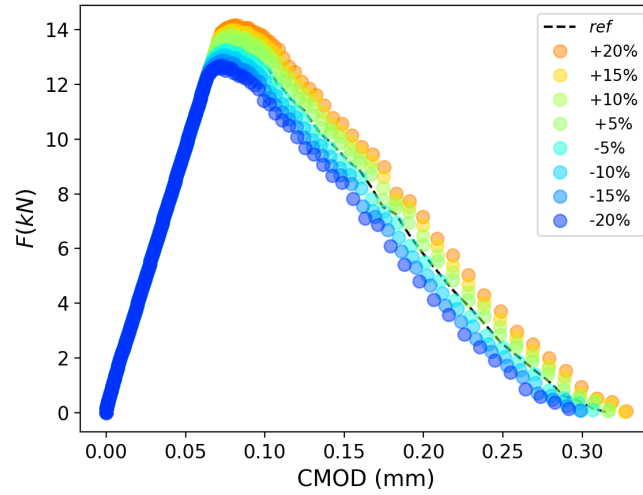


Figure 11: Comparison between the reference Load vs. CMOD curve (dash line) and the ones related to the variation of u_c of $\pm 20\%$ while u_e constant.

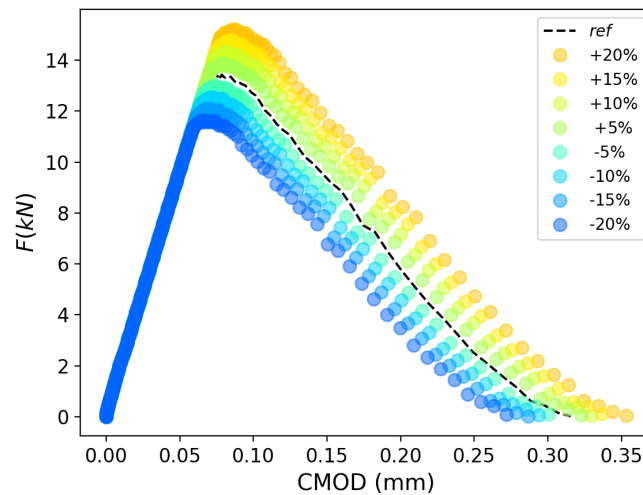


Figure 12: Comparison between the reference Load vs. CMOD curve (dash line) and the ones related to the variation of u_e of $\pm 20\%$ while u_c constant.

399 This is exhibited in Figure 12 where an increase of u_e at the local scale induces an increase of the maximal
 400 force at the macroscopic scale and a delay of the occurrence of the nonlinear response of the curves.

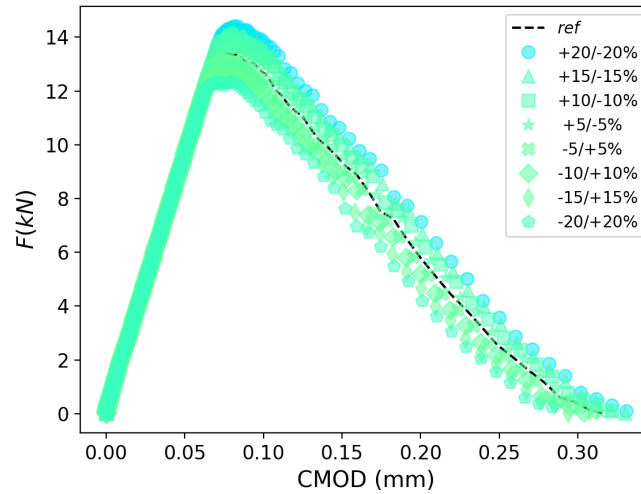


Figure 13: Comparison between the reference Load vs. CMOD curve (dash line) and the ones related to the variation of u_c and u_e of $\pm 20\%$ while w_d^0 is constant.

401 Figure 13 demonstrates that the non-linear region of the curve is also governed by the shape of the
 402 energy curve (cf. Figure 10). Although the dissipative energy in this parametric study is almost constant,
 403 we observe a variation of about 10% on the characteristic values of the response curve. So by combining
 404 the effects of u_e , u_c and the shape of the local curve (cf. Figure 10) it is possible to obtain a better optimal
 405 result to fit experiments. Thus the experimental characterization of this type of local curve depicting the
 406 micro-structural phenomenon linked to fracture is relevant and is still an ongoing problem.

407 4.3 Brazilian test

408 As a complement to the previous numerical simulation and as an opening to the continuation of the
 409 present work, the developed CZM law is used in the simulation of a Brazilian test. This test consists
 410 of compressing a circular sample located between two rigid plates. Contrary to the previous case, no
 411 pre-crack is introduced in the numerical model. The microstructure of the sample used is presented on the
 412 left side of Figure 14. This microstructure has been generated using the open-source Software Neper
 413 [Quey et al. 2011](#). It is composed of 1 000 elastic grains following a normal size distribution to make the
 414 microstructure heterogeneous [Ma et al. 2018](#). In these case, the cohesive zones are only introduced at the
 415 grain boundaries. The mesh size used for meshing is identical for all grains and calibrated so that the
 416 smallest grains have at least two elements on their smallest side. The total number of elements is 98 378. A
 417 zoom of the mesh is shown on the right hand side of Figure 14. For the sake of simplicity the diameter of
 418 the sample is unitary. A vertical velocity is imposed on both walls to compress the sample. The simulation
 419 is carried out in large deformations in order to manage possible strain localisation and grain rotations. The
 420 elastic constitutive equations are those of the linear elasticity where stresses and strains are respectively
 421 represented by the 2^{nde} Piola-Kirchoff stress tensor and the Green-Lagrange strain tensor.

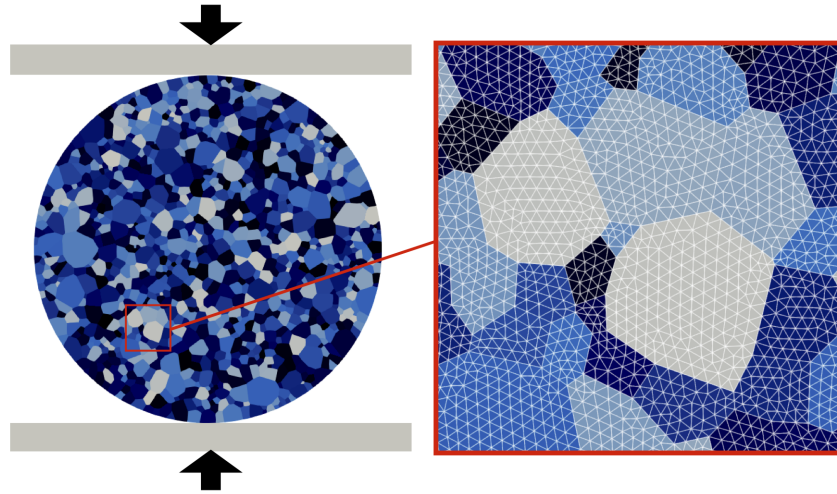


Figure 14: Visualization of the meshed microstructure used in the simulation of the Brazilian disc test

K_n^0 (N m^{-1})	α	u_e (m)	u_c (m)
$2.48 \cdot 10^{15}$	0.4	$0.8 \cdot 10^{-6}$	$1.0 \cdot 10^{-6}$

Table 2: Parameter values of the CZM

422 For homogeneous material during Brazilian test a tensile state is induced in the center of the disc
 423 perpendicular to the load direction. Increasing the load leads to an increase in tensile stress until a crack
 424 appears in the center of the disc. Under the effect of the load, the crack develops until the disc eventually
 425 separates into at least two parts. For a heterogeneous material the damage occurs near the rigid plates and
 426 then develops along the loading axis until the disk breaks [Na et al. 2017](#). Figure 15 shows a visual of the
 427 sample at the end of the simulation.

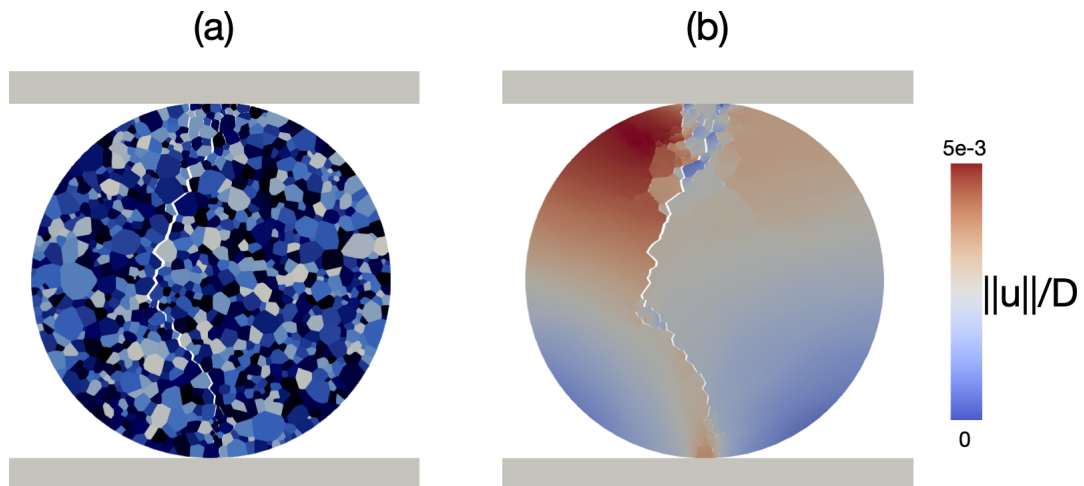


Figure 15: Final state of the simulation: Visualization of a) the crack through the microstructure and b) the norm of displacement field normalized by the value, D , of the diameter within the sample.

428 Figure 15(a) shows the macro crack zigzagging through the microstructure. This extends from the
 429 contact between the sample and the rigid plates away from the centre of the sample. Figure 15(b) shows
 430 the norm of the adimensionalized displacement field within the sample. The discontinuities within this
 431 field allow the observation of multiple cracking paths generated during compression. Numerous disjointed

432 fragments can be particularly seen in the volume near the top wall.

433 To complete these observations, the evolution of the dissipated energy fields is presented in Figure 16.
 434 The image (a) corresponds to the initiation of the crack while the image (f) corresponds to the end of the
 435 simulation. The other images are captured at intermediate times. Through the figures 16 (a) to (f) the
 436 damage evolution is exhibited where branching is observed until the coalescence of the macro crack.
 437 The next step is to experimentally perform the same type of test using an experimental setup coupling
 438 kinematic and thermal full-field measurements. The kinematic measurements will allow us to locate zones
 439 of strain localization and even discontinuities of the displacement fields while the thermal measurements
 440 will be used to determine the zones where the dissipation is localized. The confrontation of this two
 441 informations should should help us to check the relevance of this energy approach of cohesive zones.

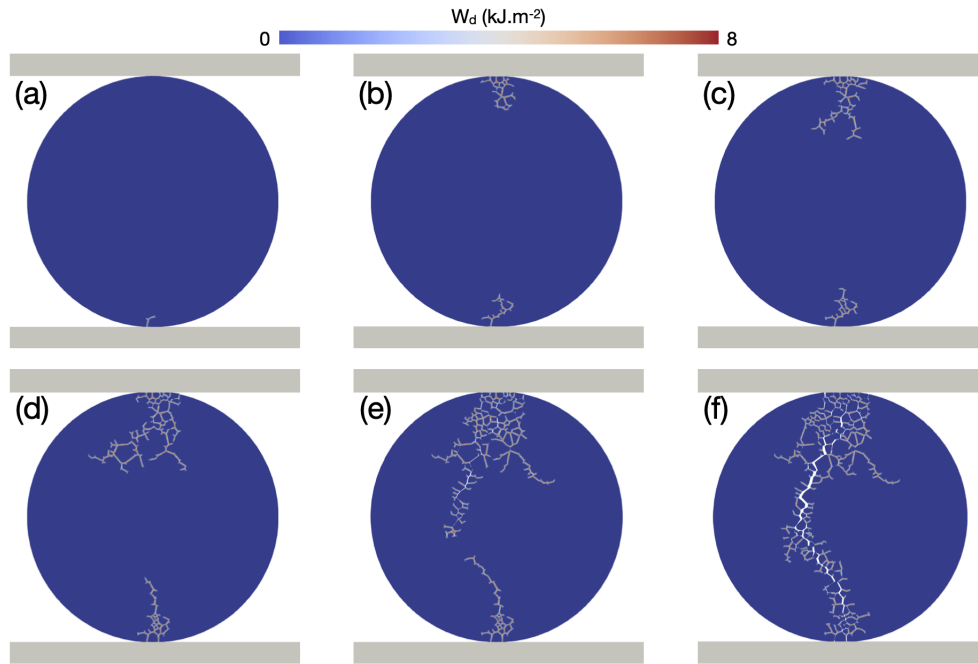


Figure 16: Evolution of the dissipated energy field from the crack initiation (a) to the end of simulation (f).

442 5 Conclusion

443 In this paper we present an energy criterion for cohesive zone models where the damage progress is
 444 assessed together with the ability of the material to store energy elastically. The damage state variable
 445 used is $u_d(t) = \text{Sup} \{u_{eq}(\tau), \tau \leq t\}$ where u_{eq} is an equivalent displacement compatible with the isotropic
 446 evolution of the damage progress. The paper shows that if damage is the unique and exclusive dissipative
 447 mechanisms, the damage evolution law is automatically fixed by the evolution of the maximum storable
 448 elastic energy $w_e^d(u_d)$. We have also underlined that the data of this energy is equivalent in a 1D formalism
 449 to the one of a traction-separation law. The interest of this energy approach is its immediate generalization
 450 to 3D cohesive zone models. In order to check the operational character of this type of approach, the
 451 isotropic damage model has been implemented in the open source software IMGc90 based on Non-Smooth
 452 Contact Dynamics (NSCD) and used to perform numerical simulations in the case of bending and Brazilian

453 tests. The results obtained for this plain stress modeling are encouraging. Using a simple quadratic function
454 $w_e^d(u_d)$ for the interface, we obtained a close correlation between the simulations and the experimental
455 observations of the crack path for the bending test, and realistic multicrack propagations in the case of the
456 Brazilian test. A parametric study of the macroscopic response of the structure naturally demonstrates the
457 importance of the shape of the function $w_e^d(u_d)$ which characterize the interface behavior between two
458 elements. It is indeed this quantity that we will have to identify experimentally. In subsequent theoretical
459 developments, first we will consider an extension to a non isotropic degradation of the material elastic
460 properties. From an experimental stand point Brazilain test will be performed by using full field techniques
461 during monotonic loadings, the goal being to extract from the experimental data valuable information on
462 the form of the energy balance and particularly on $w_e^d(u_d)$.

463 6 Bibliography

- 464 Barrenblatt, G. (1962). “The mathematical theory of equilibrium of cracks in brittle fracture”. *Adv. Appl.*
465 *Mech.* 7, pp. 55–129
- 466 Benaarbia, A. and A. Chrysochoos (2017). “Proper orthogonal decomposition preprocessing of infrared
467 images to rapidly assess stress-induced heat source fields”. *Quantitative InfraRed Thermography Journal*
468 14.1, pp. 132–152. DOI: [10.1080/17686733.2017.1281553](https://doi.org/10.1080/17686733.2017.1281553). eprint: <https://doi.org/10.1080/17686733.2017.1281553>
- 469
- 470 Blal, N., L. Daridon, Y. Monerie, and S. Pagano (2011). “Criteria on the artificial compliance inherent to the
471 intrinsic cohesive zone”. *Comptes Rendus Mécanique* 339.12, pp. 789–795. DOI: [https://doi.org/10.1016/j.](https://doi.org/10.1016/j.crme.2011.10.001)
472 [crme.2011.10.001](https://doi.org/10.1016/j.crme.2011.10.001)
- 473 Bosch, M. V. den, P. Schreurs, and M. Geers (2006). “An improved description of the exponential Xu and
474 Needleman cohesive zone law for mixed-mode decohesion”. *Engineering Fracture Mechanics* 73.9,
475 pp. 1220–1234. DOI: <https://doi.org/10.1016/j.engfracmech.2005.12.006>
- 476 Bouvard, J., J. Chaboche, F. Feyel, and F. Gallerneau (2009). “A cohesive zone model for fatigue and
477 creep-fatigue crack growth in single crystal superalloys”. *International Journal of Fatigue* 31.5, pp. 868
478 –879. DOI: <https://doi.org/10.1016/j.ijfatigue.2008.11.002>
- 479 Cendón, D., J. Gálvez, M. Elices, and J. Planas (2000). “Modelling the fracture of concrete under mixed
480 loading”. *International Journal of Fracture* 103.3, pp. 293–310. DOI: [10.1023/A:1007687025575](https://doi.org/10.1023/A:1007687025575)
- 481 Champagne, M., M. Renouf, and Y. Berthier (Jan. 2014). “Modeling Wear for Heterogeneous Bi-Phasic
482 Materials Using Discrete Elements Approach”. *Journal of Tribology* 136.2. 021603. DOI: [10.1115/1.4026053](https://doi.org/10.1115/1.4026053).
483 eprint: [https://asmedigitalcollection.asme.org/tribology/article-pdf/136/2/021603/6284756/trib_136_](https://asmedigitalcollection.asme.org/tribology/article-pdf/136/2/021603/6284756/trib_136_02_021603.pdf)
484 [_02_021603.pdf](https://asmedigitalcollection.asme.org/tribology/article-pdf/136/2/021603/6284756/trib_136_02_021603.pdf)
- 485 Chandrakanth, S. and P. Pandey (1995). “An isotropic damage model for ductile material”. *Engineering*
486 *Fracture Mechanics* 50.4, pp. 457–465. DOI: [https://doi.org/10.1016/0013-7944\(94\)00214-3](https://doi.org/10.1016/0013-7944(94)00214-3)
- 487 Chrysochoos, A. (2012). “Infrared thermography applied to the analysis of material behavior: a brief
488 overview”. *Quantitative InfraRed Thermography Journal* 9.2, pp. 193–208. DOI: [10.1080/17686733.2012.746069](https://doi.org/10.1080/17686733.2012.746069).
489 eprint: <https://doi.org/10.1080/17686733.2012.746069>
- 490 Costanzo, F. and D. Allen (1995). “A continuum thermodynamic analysis of cohesive zone models”.
491 *International Journal of Engineering Science* 33.15. The Edelen Symposium, pp. 2197–2219. DOI:
492 [https://doi.org/10.1016/0020-7225\(95\)00066-7](https://doi.org/10.1016/0020-7225(95)00066-7)
- 493 Daridon, L., B. Wattrisse, A. Chrysochoos, and M. Potier-Ferry (2011). “Solving fracture problems
494 using an asymptotic numerical method”. *Computers & Structures* 89.5, pp. 476–484. DOI: <https://doi.org/10.1016/j.compstruc.2010.12.001>
- 495
- 496 Dubois, F. and M. Jean (2006). “The non smooth contact dynamic method: recent LMGC90 software
497 developments and application”. *Analysis and Simulation of Contact Problems*. Ed. by P. Wriggers and

- 498 U. Nackenhorst. Berlin, Heidelberg: Springer Berlin Heidelberg, pp. 375–378. DOI: [10.1007/3-540-31761-](https://doi.org/10.1007/3-540-31761-9_44)
499 [9_44](https://doi.org/10.1007/3-540-31761-9_44)
- 500 Dubois, F., M. Jean, M. Renouf, R. Mozul, A. Martin, and M. Bagn eris (May 2011). “LMGC90”. *10e colloque*
501 *national en calcul des structures*. Giens, France, Cl  USB
- 502 Dugdale, D. (1960). “Yielding of steel sheets containing slits”. *Journal of the Mechanics and Physics of Solids*
503 8.2, pp. 100 –104. DOI: [https://doi.org/10.1016/0022-5096\(60\)90013-2](https://doi.org/10.1016/0022-5096(60)90013-2)
- 504 Evangelista, F., J. R. Roesler, and S. P. Proen a (2013). “Three-dimensional cohesive zone model for fracture
505 of cementitious materials based on the thermodynamics of irreversible processes”. *Engineering Fracture*
506 *Mechanics* 97, pp. 261–280
- 507 Fremond, M. (2002). *Non-smooth Thermomechanics*. Ed. by Springer. Springer-Verlag Berlin Heidelberg
- 508 Galvez, J., M. Elices, G. V. Guinea, and J. Planas (1996). “Crack trajectories under mixed mode and
509 non-proportional loading”. *International Journal of Fracture* 81.2, pp. 171–193. DOI: [10.1007/BF00033181](https://doi.org/10.1007/BF00033181)
- 510 Gurtin, M. E. (1979). “Thermodynamics and the cohesive zone in fracture”. *Zeitschrift f r angewandte*
511 *Mathematik und Physik ZAMP* 30.6, pp. 991–1003
- 512 Halphen, B. and N. Quoc-Son (1975). “Sur les mat riaux standards generalis s”. *Journal de m canique* 14,
513 pp. 39,63
- 514 Jean, M. (1999). “The non-smooth contact dynamics method”. *Computer Methods in Applied Mechanics and*
515 *Engineering* 177.3, pp. 235 –257. DOI: [https://doi.org/10.1016/S0045-7825\(98\)00383-1](https://doi.org/10.1016/S0045-7825(98)00383-1)
- 516 Jean, M., V. Acary, and Y. Monerie (2001). “Non-smooth contact dynamics approach of cohesive materials”.
517 *Philosophical Transactions of the Royal Society of London A: Mathematical, Physical and Engineering*
518 *Sciences* 359.1789, pp. 2497–2518. DOI: [10.1098/rsta.2001.0906](https://doi.org/10.1098/rsta.2001.0906). eprint: [http://rsta.royalsocietypublishing.](http://rsta.royalsocietypublishing.org/content/359/1789/2497.full.pdf)
519 [org/content/359/1789/2497.full.pdf](http://rsta.royalsocietypublishing.org/content/359/1789/2497.full.pdf)
- 520 Kachanov, L. (1986). *Introduction to continuum damage mechanics*. springer
- 521 Kondo, D., H. Weleman, and F. Cormery (2007). “Basic concepts and models in continuum damage
522 mechanics”. *Revue Europ enne de G nie Civil* 11.7-8, pp. 927–943. DOI: [10.1080/17747120.2007.9692970](https://doi.org/10.1080/17747120.2007.9692970).
523 eprint: <https://doi.org/10.1080/17747120.2007.9692970>
- 524 Kuna, M. and S. Roth (2015). “General remarks on cyclic cohesive zone models”. *International Journal of*
525 *Fracture* 196.1, pp. 147–167
- 526 Lemaitre, J. (1996). *A course on damage mechanics*. springer
- 527 Ma, Y. and H. Huang (2018). “DEM analysis of failure mechanisms in the intact Brazilian test”. *International*
528 *Journal of Rock Mechanics and Mining Sciences* 102, pp. 109–119. DOI: [https://doi.org/10.1016/j.ijrmms.](https://doi.org/10.1016/j.ijrmms.2017.11.010)
529 [2017.11.010](https://doi.org/10.1016/j.ijrmms.2017.11.010)
- 530 Mo s, N., C. Stolz, P.-E. Bernard, and N. Chevaugeon. (Apr. 2011). “A level set based model for damage
531 growth: The thick level set approach”. *International Journal for Numerical Methods in Engineering* 86.3,
532 pp. 358–380. DOI: [10.1002/nme.3069](https://doi.org/10.1002/nme.3069)

- 533 Moreau, J. J. (1988). “Unilateral Contact and Dry Friction in Finite Freedom Dynamics”. *Nonsmooth*
534 *Mechanics and Applications*. Ed. by J. J. Moreau and P. D. Panagiotopoulos. Vienna: Springer Vienna,
535 pp. 1–82. DOI: [10.1007/978-3-7091-2624-0_1](https://doi.org/10.1007/978-3-7091-2624-0_1)
- 536 Na, S., W. Sun, M. D. Ingraham, and H. Yoon (2017). “Effects of spatial heterogeneity and material anisotropy
537 on the fracture pattern and macroscopic effective toughness of Mancos Shale in Brazilian tests”. *Journal*
538 *of Geophysical Research: Solid Earth* 122.8, pp. 6202–6230. DOI: <https://doi.org/10.1002/2016JB013374>.
539 eprint: <https://agupubs.onlinelibrary.wiley.com/doi/pdf/10.1002/2016JB013374>
- 540 Needleman, A. (1990). “An analysis of tensile decohesion along an interface”. *Journal of the Mechanics and*
541 *Physics of Solids* 38.3, pp. 289–324. DOI: [https://doi.org/10.1016/0022-5096\(90\)90001-K](https://doi.org/10.1016/0022-5096(90)90001-K)
- 542 Onsager, L. (1931). “Reciprocal Relations in Irreversible Processes. I.” *Phys. Rev.* 37 (4), pp. 405–426. DOI:
543 [10.1103/PhysRev.37.405](https://doi.org/10.1103/PhysRev.37.405)
- 544 Ortiz, M. and A. Pandolfi (1999). “Finite-deformation irreversible cohesive elements for three-dimensional
545 crack-propagation analysis”. *International journal of numerical method in engineering*. 44.9, pp. 1267–
546 1282
- 547 Park, K., G. H. Paulino, and J. R. Roesler (2009). “A unified potential-based cohesive model of mixed-mode
548 fracture”. *Journal of the Mechanics and Physics of Solids* 57.6, pp. 891–908. DOI: [https://doi.org/10.1016/j.](https://doi.org/10.1016/j.jmps.2008.10.003)
549 [jmps.2008.10.003](https://doi.org/10.1016/j.jmps.2008.10.003)
- 550 Quey, R., P. Dawson, and F. Barbe (2011). “Large-scale 3D random polycrystals for the finite element
551 method: Generation, meshing and remeshing”. *Computer Methods in Applied Mechanics and Engineering*
552 200.17, pp. 1729–1745. DOI: <https://doi.org/10.1016/j.cma.2011.01.002>
- 553 Rabotnov, Y. N., F. A. Leckie, and W. Prager (Mar. 1970). “Creep Problems in Structural Members”. *Journal*
554 *of Applied Mechanics* 37.1, pp. 249–249. DOI: [10.1115/1.3408479](https://doi.org/10.1115/1.3408479). eprint: [https://asmedigitalcollection.](https://asmedigitalcollection.asme.org/appliedmechanics/article-pdf/37/1/249/5450383/249_2.pdf)
555 [asme.org/appliedmechanics/article-pdf/37/1/249/5450383/249_2.pdf](https://asmedigitalcollection.asme.org/appliedmechanics/article-pdf/37/1/249/5450383/249_2.pdf)
- 556 Richefeu, V., A. Chrysochoos, V. Huon, Y. Monerie, R. Peyroux, and B. Wattrisse (2012). “Toward local
557 identification of cohesive zone models using digital image correlation”. *European Journal of Mechanics -*
558 *A/Solids* 34. Supplement C, pp. 38–51. DOI: <https://doi.org/10.1016/j.euromechsol.2011.12.001>
- 559 Roe, K. and T. Sigmund (2003). “An irreversible cohesive zone model for interface fatigue crack growth
560 simulation”. *Engineering Fracture Mechanics* 70.2, pp. 209–232. DOI: [https://doi.org/10.1016/S0013-](https://doi.org/10.1016/S0013-7944(02)00034-6)
561 [7944\(02\)00034-6](https://doi.org/10.1016/S0013-7944(02)00034-6)
- 562 Serpieri, R., E. Sacco, and G. Alfano (2015a). “A thermodynamically consistent derivation of a frictional-
563 damage cohesive-zone model with different mode I and mode II fracture energies”. *European Journal of*
564 *Mechanics - A/Solids* 49, pp. 13–25
- 565 Serpieri, R., E. Sacco, and G. Alfano (2015b). “A thermodynamically consistent derivation of a frictional-
566 damage cohesive-zone model with different mode I and mode II fracture energies”. *European Journal of*
567 *Mechanics - A/Solids* 49, pp. 13–25. DOI: <https://doi.org/10.1016/j.euromechsol.2014.06.006>

- 568 Shu, W. and I. Stanciulescu (2020). “Fully coupled thermo-mechanical cohesive zone model with thermal
569 softening: Application to nanocomposites”. *International Journal of Solids and Structures* 188-189,
570 pp. 1–11
- 571 Wojtacki, K., L. Daridon, F. Dubois, N. N. Moës, and Y. Monerie (2015). “Analyse comparative de trois
572 méthodes performantes de simulation numérique de la fissuration”. 13e colloque national en calcul des
573 structures - CSMA
- 574 Zener, C. (1938). “Internal Friction in Solids II. General Theory of Thermoelastic Internal Friction”. *Phys.*
575 *Rev.* 53 (1), pp. 90–99. DOI: [10.1103/PhysRev.53.90](https://doi.org/10.1103/PhysRev.53.90)